

Smoothed particle hydrodynamics with radiative transfer in the flux-limited diffusion approximation

Stuart C. Whitehouse and Matthew R. Bate*

School of Physics, University of Exeter, Stocker Road, Exeter EX4 4QL

Accepted for publication in MNRAS

ABSTRACT

We describe the implementation and testing of a smoothed particle hydrodynamics (SPH) code that solves the equations of radiation hydrodynamics in the flux-limited diffusion (FLD) approximation. The SPH equations of radiation hydrodynamics for an explicit integration scheme are derived and tested. We also discuss the implementation of an implicit numerical scheme for solving the radiation equations that allows the system to be evolved using timesteps much longer than the explicit radiation timestep. The code is tested on a variety of one-dimensional radiation hydrodynamics problems including radiation propagating in an optically thin medium, optically thick and thin shocks, subcritical and supercritical radiating shocks, and a radiation dominated shock. Many of the tests were also performed by Turner & Stone (2001) to test their implementation of a FLD module for the ZEUS-2D code. The SPH code performs at least as well as the ZEUS-2D code in these tests.

Key words: hydrodynamics – methods: numerical – radiative transfer.

1 INTRODUCTION

The smoothed particle hydrodynamics (SPH) technique was first introduced by Lucy (1977) and Gingold & Monaghan (1977) as a Lagrangian method for solving astrophysical fluid dynamics problems. Over the subsequent years, it has been used to investigate a wide range of astronomical problems including galaxy formation, star formation, stellar collisions, supernova explosions, and meteor impacts (see Monaghan 1992, for a review). It has also made its way into other fields of science and engineering, having been used to model tsunamis, volcanic eruptions, and ballistics.

Many improvements and extensions to the method have been made over the years. Particle smoothing lengths that varied in space as well as time were introduced (Evrard 1988; Hernquist & Katz 1989; Benz et al. 1990) to allow the spatial resolution of the method to vary with density. This feature allows SPH to compete against the more modern adaptive mesh refinement (AMR) codes. Gravity, while naturally requiring a computational effort scaling as the square of the particle number N , was reduced to order $N \log N$ scaling using hierarchical tree structures (Hernquist & Katz 1989; Benz et al. 1990). Recently, a reformulation of the SPH equations has allowed both energy and entropy to be conserved simultaneously (Inutsuka & Imaeda 2001; Springel & Hernquist 2002; Monaghan 2002). Finally, many authors have suggested various reformulations of SPH's artificial viscosity (Wood 1981; Gingold & Monaghan 1983; Evrard 1988; Balsara, D. 1989; Flebbe et al. 1994; Watkins et al. 1996; Morris & Monaghan 1997) or its elimination in favour of Godunov schemes (Inutsuka 1994; Inutsuka, S.- I. 1998; Inutsuka & Imaeda 2001; Cha, S.- H. 2002; Cha & Whitworth 2003).

However, with a few exceptions, SPH is primarily used to model pure hydrodynamics. Incorporating magnetic fields into the SPH formalism has proven difficult. Problems encountered include numerical tensional instabilities, non-conservation of momentum, and/or not enforcing the divergence of the magnetic field to be zero (see the introduction of Price & Monaghan 2004a). Recently, a promising new method was presented by Price & Monaghan (2004a,b) which may at last overcome these problems.

Similarly, SPH has been used for radiation hydrodynamics (Lucy 1977; Brookshaw 1985, 1986), but not without encountering problems. Boundary conditions that allow appropriate heat losses can be difficult to implement. More importantly,

* E-mail: scw@astro.ex.ac.uk, mbate@astro.ex.ac.uk

the radiation equations involve the second spatial derivative of the radiation energy density. In the standard SPH formalism, the spatial derivative of a quantity is calculated using a sum over neighbouring particles, introducing noise. Calculating a second spatial derivative from such a first derivative produces a result that is very sensitive to particle disorder. In addition, for many interesting astrophysical problems, the timestep required to evolve the radiation equations explicitly is many orders of magnitude shorter than the dynamical timescale of the problem. Another recent approach to solving radiation transport with SPH is to combine SPH with Monte-Carlo radiative transfer (Oxley & Woolfson 2003). This has the advantage that the radiative transfer is not carried out using the SPH formalism; the radiative transfer is calculated between hydrodynamical timesteps and the resulting temperatures are applied to the SPH particles. Since the method involves following photon packets, it is simple to include radiating point sources (e.g. stars) and scattering, and it allows frequency-dependent radiative transfer. Its main disadvantages are that it assumes the matter and radiation temperatures are the same and it is exceedingly computationally expensive, especially in the optically thick regime.

Recently, Cleary & Monaghan (1999) published a method for modelling heat conduction with SPH. The heat conduction equation is similar in form to the equation for radiative diffusion. Cleary & Monaghan's method avoids the sensitivity to particle disorder by reformulating the heat conduction equation to use a first-order rather than second-order spatial derivative. This solves one of the hinderances for implementing radiative transfer within the SPH formalism. Jubelgas, Springel & Dolag (2004) recently used this method to study heat conduction in galaxy clusters.

In this paper, we describe the implementation of an SPH code that solves the equations of radiation hydrodynamics in the flux-limited diffusion approximation. The flux-limited diffusion approximation is briefly reviewed in Section 2. Section 3 describes the SPH implementation in detail. Section 4 presents the results of various test calculations using the code. Our conclusions and some directions for future development are summarised in Section 5.

2 EQUATIONS OF RADIATION HYDRODYNAMICS

In a frame comoving with a radiating fluid, assuming local thermodynamic equilibrium (LTE), the coupled equations of radiation hydrodynamics (RHD) to order unity in v/c are

$$\frac{D\rho}{Dt} + \rho \nabla \cdot \mathbf{v} = 0, \quad (1)$$

$$\rho \frac{D\mathbf{v}}{Dt} = -\nabla p + \frac{\chi_F \rho}{c} \mathbf{F}, \quad (2)$$

$$\rho \frac{D}{Dt} \left(\frac{E}{\rho} \right) = -\nabla \cdot \mathbf{F} - \nabla \mathbf{v} \cdot \mathbf{P} + 4\pi \kappa_P \rho B - c \kappa_E \rho E, \quad (3)$$

$$\rho \frac{D}{Dt} \left(\frac{e}{\rho} \right) = -p \nabla \cdot \mathbf{v} - 4\pi \kappa_P \rho B + c \kappa_E \rho E, \quad (4)$$

$$\frac{\rho}{c^2} \frac{D}{Dt} \left(\frac{\mathbf{F}}{\rho} \right) = -\nabla \cdot \mathbf{P} - \frac{\chi_F \rho}{c} \mathbf{F} \quad (5)$$

(Mihalas & Mihalas 1984; Turner & Stone 2001). In these equations, $D/Dt \equiv \partial/\partial t + \mathbf{v} \cdot \nabla$ is the convective derivative. The symbols ρ , e , \mathbf{v} , and p , represent the material mass density, energy density, velocity, and scalar isotropic pressure, respectively. The total frequency-integrated radiation energy density, momentum density or flux, and pressure tensor are represented by E , \mathbf{F} , and \mathbf{P} , respectively. These are the zeroth, first and second angular moments of the radiation specific intensity which, in general, varies with spatial position, viewing direction, frequency, and time.

A full description of the flux-limited diffusion approximation to the above equations is given by Turner & Stone (2001). Here we simply summarise the main points. The assumption of LTE allows the rate of emission of radiation from the matter in equations 3 and 4 to be written as the Planck function, B . Equations 2 to 5 have been integrated over frequency, leading to the flux mean total opacity χ_F , and the Planck mean and energy mean absorption opacities, κ_P and κ_E . In this paper, the opacities are assumed to be independent of frequency so that $\kappa_P = \kappa_E$ and the subscripts may be omitted. The total opacity, χ , is the sum of components due to absorption, κ , and scattering, σ . Note that the above opacities have dimensions of length squared over mass (i.e. cm^2/g) whereas Turner & Stone (2001) define their opacities to have dimensions of inverse length (i.e. their opacities are equal to ours multiplied by the density).

The equations of RHD may be closed by an equation of state specifying the gas pressure, the addition of constitutive relations for the Planck function and opacities, and an assumption about the relationship between the angular moments of the radiation field. In this paper, we use an ideal equation of state for the gas pressure $p = (\gamma - 1)u\rho$, where $u = e/\rho$ is the specific energy of the gas. Thus, the temperature of the gas is $T_g = (\gamma - 1)\mu u/R_g = u/c_v$ where μ is the dimensionless mean particle mass, R_g is the gas constant, and c_v is the specific heat capacity of the gas. The Planck function $B = (\sigma_B/\pi)T_g^4$,

where σ_B is the Stefan-Boltzmann constant. The radiation energy density also has an associated temperature T_r from the equation $E = 4\sigma_B T_r^4/c$.

When the radiation field is isotropic $P = \frac{1}{3}E$. The Eddington approximation assumes this relation holds everywhere and implies that, in a steady state, equation 5 becomes

$$\mathbf{F} = -\frac{c}{3\chi\rho}\nabla E. \quad (6)$$

This expression gives the correct flux in optically thick regions, where $\chi\rho$ is large. However, in optically thin regions where $\chi\rho \rightarrow 0$ the flux tends to infinity whereas in reality $|\mathbf{F}| \leq cE$. Flux-limited diffusion solves this problem by limiting the flux in optically thin environment to always obey the above inequality. Levermore & Pomraning (1981) wrote the radiation flux in the form of Fick's law of diffusion as

$$\mathbf{F} = -D\nabla E, \quad (7)$$

with a diffusion constant given by

$$D = \frac{c\lambda}{\chi\rho}. \quad (8)$$

The dimensionless function $\lambda(E)$ is called the flux limiter. The radiation pressure tensor may then be written in terms of the radiation energy density as

$$\mathbf{P} = \mathbf{f}E, \quad (9)$$

where the components of the Eddington tensor, \mathbf{f} , are given by

$$\mathbf{f} = \frac{1}{2}(1-f)\mathbf{I} + \frac{1}{2}(3f-1)\hat{\mathbf{n}}\hat{\mathbf{n}}, \quad (10)$$

where $\hat{\mathbf{n}} = \nabla E/|\nabla E|$ is the unit vector in the direction of the radiation energy density gradient and the dimensionless scalar function $f(E)$ is called the Eddington factor. The flux limiter and the Eddington factor are related by

$$f = \lambda + \lambda^2 R^2, \quad (11)$$

where R is the dimensionless quantity $R = |\nabla E|/(\chi\rho E)$.

Equations 7 to 11 close the equations of RHD, eliminating the need to solve equation 5. However, we must still choose an expression for the flux limiter, λ . In this paper, we choose Levermore & Pomraning's flux limiter

$$\lambda(R) = \frac{2+R}{6+3R+R^2}. \quad (12)$$

to allow direct comparison of our results with those of Turner & Stone (2001). In the optically thin limit

$$\lim_{R \rightarrow \infty} \lambda(R) = \frac{1}{R} \quad (13)$$

to first order in R^{-1} so the magnitude of the flux approaches $|\mathbf{F}| = c|\nabla E|/(\chi\rho R) = cE$, as required. In the optically thick or diffusion limit

$$\lim_{R \rightarrow 0} \lambda(R) = \frac{1}{3} \quad (14)$$

to first order in R , so the flux takes the value given by equation 6. Many other forms of flux limiter have been developed to give more realistic performances on different problems (see Turner & Stone 2001 and references therein).

3 NUMERICAL METHOD

The radiation terms in equations 2 to 4 are added to a one-dimensional SPH code that is otherwise standard (e.g. Benz et al. 1990; Monaghan 1992). The usual hydrodynamical SPH equations will not be rederived here. We use the standard cubic spline kernel, W , for the SPH summations over particles. The smoothing lengths of particles vary in time and space, subject to the constraint that the number of neighbours for each particle remains approximately constant at $N_{\text{neigh}} = 8$. The smoothing length for particle i is given by

$$h_i = \frac{1}{2}\text{MAX}(|x_i - x_{i+5}| + |x_i - x_{i+4}|, |x_i - x_{i-5}| + |x_i - x_{i-4}|), \quad (15)$$

where x_i is the position of particle i , and x_{i+4} and x_{i+5} are the positions of the fourth and fifth closest particles in the positive x direction, and x_{i-4} and x_{i-5} are the positions of the fourth and fifth closest particles in the negative x direction.

The SPH equations are integrated using one of two possible integrators: a predictor-corrector integrator, or a second-order Runge-Kutta-Fehlberg integrator. All particles are advanced with the same timestep. The integrators give essentially

identical results, so we only present the results of the test calculations using one of the integrators, the second-order Runge-Kutta-Fehlberg integrator. We use the standard form of artificial viscosity (Gingold & Monaghan 1983; Monaghan 1992) with strength parameters $\alpha_v = 1$ and $\beta_v = 2$ unless otherwise stated. The code does not include gravity or magnetic fields.

3.1 Explicit SPH formulation of the radiation equations

As SPH is a Lagrangian method, it is natural to use specific energies for the gas and radiation. The specific energy of the gas is $u = e/\rho$ and we define the specific radiation energy to be $\xi = E/\rho$. Equation 1 does not need to be solved directly since the density of each particle is calculated using the standard SPH summation over the particle and its neighbours. Equations 2 to 4 can then be written

$$\frac{D\mathbf{v}}{Dt} = -\frac{\nabla p}{\rho} + \frac{\chi}{c} \mathbf{F}, \quad (16)$$

$$\frac{D\xi}{Dt} = -\frac{\nabla \cdot \mathbf{F}}{\rho} - \frac{\nabla \mathbf{v} \cdot \mathbf{P}}{\rho} - a c \kappa \left(\frac{\rho \xi}{a} - \left(\frac{u}{c_v} \right)^4 \right), \quad (17)$$

$$\frac{Du}{Dt} = -\frac{p \nabla \cdot \mathbf{v}}{\rho} + a c \kappa \left(\frac{\rho \xi}{a} - \left(\frac{u}{c_v} \right)^4 \right), \quad (18)$$

where $a = 4\sigma_B/c$. The first terms on the right-hand sides of each of equations 16 and 18 are the hydrodynamic terms and are solved in the usual SPH manner (see below).

The first term on the right-hand side of equation 17 is the radiation flux term which, as discussed in Section 2, is given by

$$-\frac{\nabla \cdot \mathbf{F}}{\rho} = \frac{1}{\rho} \nabla \cdot \left(\frac{c \lambda}{\kappa \rho} \nabla E \right). \quad (19)$$

This has a similar form to the right-hand side of the equation for heat conduction

$$\frac{du}{dt} = \frac{1}{\rho} \nabla \cdot (k \nabla T_m), \quad (20)$$

where k is the thermal conductivity. These equations both involve second-order spatial derivatives. As mentioned in the introduction, direct computation of a second-order derivative using standard SPH techniques makes the result extremely sensitive to particle disorder, and may result in unstable integration. Cleary & Monaghan (1999) overcome this difficulty by reformulating the second-order derivative as a first-order derivative using a Taylor series expansion. A full description of this reformulation is given by Jubelgas et al. (2004). The heat conduction equation in SPH formalism then becomes

$$\frac{du_i}{dt} = \sum_{j=1}^N \frac{m_j}{\rho_i \rho_j} \left(\frac{4 k_i k_j}{k_i + k_j} \right) (T_i - T_j) \frac{\nabla W_{ij}}{r_{ij}}, \quad (21)$$

where $W_{ij} = W(r_{ij}, h_{ij})$ with $\mathbf{r}_{ij} = \mathbf{r}_i - \mathbf{r}_j$ and $h_{ij} = (h_i + h_j)/2$, and the subscripts denote particles i and j . Hence, the SPH formulation of equation 19 is

$$\left(\frac{D\xi_i}{Dt} \right)_{\text{flux}} = \sum_{j=1}^N \frac{m_j}{\rho_i \rho_j} c \left[\frac{\frac{4 \lambda_i}{\kappa_i \rho_i} \frac{\lambda_j}{\kappa_j \rho_j}}{\left(\frac{\lambda_i}{\kappa_i \rho_i} + \frac{\lambda_j}{\kappa_j \rho_j} \right)} \right] (\rho_i \xi_i - \rho_j \xi_j) \frac{\nabla W_{ij}}{r_{ij}}. \quad (22)$$

Because energy is transferred between pairs of particles, this formulation ensures that energy is conserved.

The last terms in equations 17 and 18 control the interaction between the radiation and the gas. Note that these terms are identical except in sign, indicating that energy is conserved. They are of the form $T_r^4 - T_g^4$, as $\xi = a T_r^4 / \rho$ and $u = c_v T_g$, similar to that of Black & Bodenheimer (1975) except for our use of specific energies rather than energy densities.

In one dimension, the radiation pressure term in equation 18 becomes

$$\left(\frac{D\xi_i}{Dt} \right)_{\text{radpres}} = -\frac{1}{\rho} \nabla \mathbf{v} : \mathbf{P} = -(\nabla \cdot \mathbf{v})_i f_i \xi_i, \quad (23)$$

where the Eddington factor is

$$f_i = \lambda_i + \lambda_i^2 \left(\frac{|\nabla(\rho_i \xi_i)|}{\kappa_i \rho_i^2 \xi_i} \right)^2. \quad (24)$$

The final SPH formulations of equations 17 and 18 are

$$\frac{D\xi_i}{Dt} = -(\nabla \cdot \mathbf{v})_i f_i \xi_i + \sum_{j=1}^N \frac{m_j}{\rho_i \rho_j} c \left[\frac{\frac{4 \lambda_i}{\kappa_i \rho_i} \frac{\lambda_j}{\kappa_j \rho_j}}{\left(\frac{\lambda_i}{\kappa_i \rho_i} + \frac{\lambda_j}{\kappa_j \rho_j} \right)} \right] (\rho_i \xi_i - \rho_j \xi_j) \frac{\nabla W_{ij}}{r_{ij}} - a c \kappa_i \left(\frac{\rho_i \xi_i}{a} - \left(\frac{u_i}{c_{v,i}} \right)^4 \right), \quad (25)$$

$$\frac{Du_i}{Dt} = \frac{1}{2} \sum_{j=1}^N \left(\frac{p_i}{\rho_i^2} + \frac{p_j}{\rho_j^2} + \Pi_{ij} \right) m_j \mathbf{v}_{ij} \cdot \nabla W_{ij} + ac\kappa_i \left(\frac{\rho_i \xi_i}{a} - \left(\frac{u_i}{c_{v,i}} \right)^4 \right), \quad (26)$$

where $\mathbf{v}_{ij} = \mathbf{v}_i - \mathbf{v}_j$, and the first term in equation 26 is the standard SPH expression for the hydrodynamical energy term $p(\nabla \cdot \mathbf{v})/\rho$ when the thermodynamic variable of integration is energy. We note that the radiation terms can easily be expressed in terms of entropy if one wishes to add them to the SPH formalism of Springel & Hernquist (2002). We use the standard SPH artificial viscosity

$$\Pi_{ij} = \begin{cases} \left(-\alpha_v c_s \mu_{ij} + \beta_v \mu_{ij}^2 \right) / \rho_{ij} & \text{if } \mathbf{v}_{ij} \cdot \mathbf{r}_{ij} \leq 0, \text{ and} \\ 0 & \text{if } \mathbf{v}_{ij} \cdot \mathbf{r}_{ij} > 0. \end{cases}$$

where $\mu_{ij} = h(\mathbf{v}_i - \mathbf{v}_j) \cdot (\mathbf{r}_i - \mathbf{r}_j) / (|\mathbf{r}_i - \mathbf{r}_j|^2 + \eta^2)$, with $\eta^2 = 0.01h^2$ to prevent numerical divergences if particles get too close together.

The full SPH expression of the momentum equation 16 is

$$\frac{D\mathbf{v}_i}{Dt} = - \sum_{j=1}^N m_j \left(\frac{p_i}{\rho_i^2} + \frac{p_j}{\rho_j^2} + \Pi_{ij} \right) \nabla W(r_{ij}, h_{ij}) - \frac{\lambda_i}{\rho_i} \sum_{j=1}^N m_j \xi_j \nabla W(r_{ij}, h_{ij}), \quad (27)$$

where the first term is the standard hydrodynamical term and the second term is due to radiation pressure.

3.1.1 Explicit timestep criteria

Explicit integration requires that the timesteps obey the Courant conditions for both the hydrodynamic and radiation processes. The usual hydrodynamical SPH timestep criteria are

$$dt_{\text{Courant},i} = \frac{\zeta h_i}{c_s + h_i |\nabla \cdot \mathbf{v}|_i + 1.2 (\alpha_v c_s + \beta_v h_i |\nabla \cdot \mathbf{v}|_i)}, \quad (28)$$

and

$$dt_{\text{force},i} = \zeta \sqrt{\frac{h_i}{|\mathbf{a}_i|}}, \quad (29)$$

where we use a Courant number of $\zeta = 0.3$ and \mathbf{a}_i is the acceleration of particle i . With radiation hydrodynamics, we modify equation 28 so that the sound speed c_s used for computing the timestep includes the contribution from radiation pressure, and is given by $c_s = [\max(\gamma, \frac{4}{3}) \frac{P_{\text{tot}}}{\rho}]^{\frac{1}{2}}$, where P_{tot} is the sum of both the gas and the magnitude of the radiation pressure, except where the sound speed is used as part of the viscosity, where it remains based on just the gas pressure. The radiation terms in the energy and momentum equations require additional constraints. The flux diffusion timestep is

$$dt_{\text{rad},i} = \zeta \frac{h_i^2 \rho_i \kappa_i}{c \lambda_i}. \quad (30)$$

The timestep associated with the radiation pressure term in equation 25 is simply

$$dt_{\text{radpres},i} = \zeta \frac{1}{f_i \rho_i \xi_i (\nabla \cdot \mathbf{v})_i}. \quad (31)$$

The timestep for the effect of radiation pressure on the momentum equation is taken care of already by the standard SPH force timestep criterion. The two timesteps for the interaction between radiation and matter are

$$dt_{\text{int}\xi,i} = \zeta \frac{\xi_i}{a c \kappa_i \left| \frac{\rho_i \xi_i}{a} - \left(\frac{u_i}{c_{v,i}} \right)^4 \right|}, \quad (32)$$

and

$$dt_{\text{intU},i} = \zeta \frac{u_i}{a c \kappa_i \left| \frac{\rho_i \xi_i}{a} - \left(\frac{u_i}{c_{v,i}} \right)^4 \right|}. \quad (33)$$

In cases where particles start off in thermal equilibrium ($T_g = T_r$), we found it was sometimes necessary to limit the timesteps further to ensure that too large a timestep was not used initially. In these cases, we also limited the timestep using $dt_{\text{int}\xi,i} = \zeta \xi_i / (a c \kappa_i \frac{\rho_i \xi_i}{a})$, $dt_{\text{int}\xi,i} = \zeta \xi_i / (a c \kappa_i \left(\frac{u_i}{c_{v,i}} \right)^4)$, $dt_{\text{intU},i} = \zeta u_i / (a c \kappa_i \frac{\rho_i \xi_i}{a})$ and $dt_{\text{intU},i} = \zeta u_i / (a c \kappa_i \left(\frac{u_i}{c_{v,i}} \right)^4)$.

3.2 Implicit integration

Because the speed of light is typically much larger than the hydrodynamical velocity, the timestep obtained from the Courant condition for these radiative processes is much smaller than that for the pure hydrodynamics. It is therefore desirable to integrate the radiative transfer implicitly so that a much larger timestep can be taken.

Monaghan (1997) described an implicit integration scheme for handling the interaction between dust and gas particles in an SPH code. This is an iterative method that involves sweeping over all pairs of neighbouring particles a number of times. In Monaghan's case, the drag term between gas and dust particles was integrated implicitly. Here, the radiation and gas energy equations are integrated implicitly. Monaghan tried both backward Euler and two-step implicit integration methods Monaghan (1997, section 4). We tried both of these methods and the standard trapezoidal method. We found the backward Euler and trapezoidal methods gave similar results, but that the two-step method did not converge in the limit of a large number of sweeps. Since the trapezoidal method is the most accurate A-stable second-order linear multistep method (Dahlquist 1963), we chose to use this scheme.

For the integration between a time $t = n$ and $t = n + 1$ this scheme states that for a variable $A(t)$,

$$A_i^{n+1} = A_i^n + \frac{dt}{2} \left(\frac{dA_i^n}{dt} + \frac{dA_i^{n+1}}{dt} \right), \quad (34)$$

where A^n and A^{n+1} indicate the value of A at times $t = n$ and $t = n + 1$, respectively.

We also tried an iterative scheme based on the alternating-direction implicit (ADI) scheme used by Black & Bodenheimer (1975) and Turner & Stone (2001), where progressively larger pseudo-timesteps are used between sweeps. However, testing showed that it was slower than the implicit method used below.

3.2.1 Implicit flux diffusion

Implicit integration of the radiation flux term can be performed by considering the interaction between two SPH particles i and j . According to the trapezoidal scheme

$$\xi_i^{n+1} = \xi_i^n + \frac{1}{2} \frac{dt}{N} \left[\frac{m_j}{\rho_i \rho_j} b \left(\rho_i \xi_i^n - \rho_j \xi_j^n + \rho_i \xi_i^{n+1} - \rho_j \xi_j^{n+1} \right) \frac{\nabla W_{ij}}{r_{ij}} \right] \quad (35)$$

where $b = \left[\frac{4 \frac{\lambda_i}{\kappa_i \rho_i} \frac{\lambda_j}{\kappa_j \rho_j}}{\left(\frac{\lambda_i}{\kappa_i \rho_i} + \frac{\lambda_j}{\kappa_j \rho_j} \right)} \right]$ for brevity, and N is the total number of sweeps. Similarly for particle j

$$\xi_j^{n+1} = \xi_j^n + \frac{1}{2} \frac{dt}{N} \left[\frac{m_i}{\rho_i \rho_j} b \left(\rho_j \xi_j^n - \rho_i \xi_i^n + \rho_j \xi_j^{n+1} - \rho_i \xi_i^{n+1} \right) \frac{\nabla W_{ij}}{r_{ij}} \right]. \quad (36)$$

It is possible to solve this set of equations for the quantity $\rho_i \xi_i^{n+1} - \rho_j \xi_j^{n+1}$. The solution is

$$\rho_i \xi_i^{n+1} - \rho_j \xi_j^{n+1} = (\rho_i \xi_i^n - \rho_j \xi_j^n) \left(\frac{1 + \frac{1}{2} \frac{dt}{N} b \frac{\nabla W_{ij}}{r_{ij}} \left(\frac{m_i}{\rho_i} + \frac{m_j}{\rho_j} \right)}{1 - \frac{1}{2} \frac{dt}{N} b \frac{\nabla W_{ij}}{r_{ij}} \left(\frac{m_i}{\rho_i} + \frac{m_j}{\rho_j} \right)} \right). \quad (37)$$

This is then substituted into equations 35 and 36 to provide the new values of the specific radiation energies of particles i and j . Performing a sweep involves calculating this interaction between all particle pairs. We tried both updating the energies after every interaction, and saving the changes from each interaction and updating the energies with them after all pairs had been considered. There was no significant difference between the two methods; we used the latter method since it minimizes truncation error.

3.2.2 Implicit pressure and viscous force

The $p \nabla \cdot v$ and viscous contribution to the matter energy equation should also be done implicitly. Using the same technique as above, the interaction of particle j with particle i is

$$u_i^{n+1} = u_i^n + \frac{1}{2} \frac{dt}{N} \left[\frac{1}{2} \left(\frac{(\gamma - 1) u_i^n}{\rho_i} + \frac{(\gamma - 1) u_j^n}{\rho_j} + \Pi_{ij} \right) m_j v_{ij} \nabla W_{ij} + \frac{1}{2} \left(\frac{(\gamma - 1) u_i^{n+1}}{\rho_i} + \frac{(\gamma - 1) u_j^{n+1}}{\rho_j} + \Pi_{ij} \right) m_j v_{ij} \nabla W_{ij} \right], \quad (38)$$

and vice versa for the effect of i on j . Solving for $u_i^{n+1}/\rho_i + u_j^{n+1}/\rho_j$, we obtain

$$\left(\frac{u_i^{n+1}}{\rho_i} + \frac{u_j^{n+1}}{\rho_j} \right) = \left(\frac{u_i^n}{\rho_i} + \frac{u_j^n}{\rho_j} \right) + \quad (39)$$

$$\begin{aligned} \frac{dt}{N\rho_i} \left[\frac{1}{2} \Pi_{ij} v_{ij} m_j \nabla W_{ij} + \frac{(\gamma-1)}{4} \left(\frac{u_i^n}{\rho_i} + \frac{u_j^n}{\rho_j} \right) m_j v_{ij} \nabla W_{ij} + \frac{(\gamma-1)}{4} \left(\frac{u_i^{n+1}}{\rho_i} + \frac{u_j^{n+1}}{\rho_j} \right) m_j v_{ij} \nabla W_{ij} \right] + \\ \frac{dt}{N\rho_j} \left[\frac{1}{2} \Pi_{ji} v_{ji} m_i \nabla W_{ji} + \frac{(\gamma-1)}{4} \left(\frac{u_j^n}{\rho_j} + \frac{u_i^n}{\rho_i} \right) m_i v_{ji} \nabla W_{ji} + \frac{(\gamma-1)}{4} \left(\frac{u_j^{n+1}}{\rho_j} + \frac{u_i^{n+1}}{\rho_i} \right) m_i v_{ji} \nabla W_{ji} \right]. \end{aligned}$$

Noting that $v_{ij} \nabla W_{ij} = v_{ji} \nabla W_{ji}$, and that $\Pi_{ij} = \Pi_{ji}$, this can be solved by defining four quantities:

$$\begin{aligned} c_1 &= \frac{u_i^n}{\rho_i} + \frac{dt}{2N\rho_i} \Pi_{ij} v_{ij} m_j \nabla W_{ij} + \frac{dt}{N} \frac{(\gamma-1)}{4\rho_i} \left(\frac{u_i^n}{\rho_i} + \frac{u_j^n}{\rho_j} \right) m_j v_{ij} \nabla W_{ij}, \\ c_2 &= \frac{u_j^n}{\rho_j} + \frac{dt}{2N\rho_j} \Pi_{ij} v_{ij} m_i \nabla W_{ji} + \frac{dt}{N} \frac{(\gamma-1)}{4\rho_j} \left(\frac{u_i^n}{\rho_i} + \frac{u_j^n}{\rho_j} \right) m_i v_{ji} \nabla W_{ji}, \\ c_3 &= \frac{dt}{N} \frac{(\gamma-1)}{4\rho_i} m_j v_{ij} \nabla W_{ij}, \\ c_4 &= \frac{dt}{N} \frac{(\gamma-1)}{4\rho_j} m_i v_{ji} \nabla W_{ji}, \end{aligned}$$

and the solution for $u_i^{n+1}/\rho_i + u_j^{n+1}/\rho_j$ is simply

$$u_i^{n+1}/\rho_i + u_j^{n+1}/\rho_j = \frac{c_1 + c_2}{1 - c_3 - c_4}. \quad (40)$$

This quantity is then substituted into equation 38 and its counterpart for j to provide new values of u_i and u_j . Note that in fact the viscosity has a dependence on u , as the SPH viscosity involves the sound speed $c_s \propto \sqrt{u}$. However, we neglect this weak dependence during a sweep in order to simplify the mathematics, and simply update the sound speed in advance of the next sweep. We have not noticed any significant effect of this small approximation.

3.2.3 Implicit radiation pressure

The radiation pressure term in equation 25 merely involves the divergence of the velocity, and can easily be implicitly integrated thus:

$$\xi_i^{n+1} = \xi_i^n - \frac{1}{2} \frac{dt}{N} (\nabla \cdot \mathbf{v})_i (\xi_i^{n+1} + \xi_i^n) f_i, \quad (41)$$

whose solution is

$$\xi_i^{n+1} = \xi_i^n \left(\frac{\left(1 - \frac{1}{2} \frac{dt}{N} (\nabla \cdot \mathbf{v})_i f_i \right)}{\left(1 + \frac{1}{2} \frac{dt}{N} (\nabla \cdot \mathbf{v})_i f_i \right)} \right). \quad (42)$$

3.2.4 Implicit radiation-matter interaction terms

The implicit solution of the interaction terms between ξ and u for a given particle i involves the solution of a quartic (fourth-order polynomial) equation, which is non-trivial. The equations for ξ and u are

$$\xi_i^{n+1} = \xi_i^n - \frac{1}{2} \frac{dt}{N} ac \left(\frac{\rho_i \kappa_i}{a} \xi_i^n - \frac{\kappa_i}{c_{v,i}^4} (u_i^n)^4 + \frac{\rho_i \kappa_i}{a} \xi_i^{n+1} - \frac{\kappa_i}{c_{v,i}^4} (u_i^{n+1})^4 \right) \quad (43)$$

and

$$u_i^{n+1} = u_i^n + \frac{1}{2} \frac{dt}{N} ac \left(\frac{\rho_i \kappa_i}{a} \xi_i^n - \frac{\kappa_i}{c_{v,i}^4} (u_i^n)^4 + \frac{\rho_i \kappa_i}{a} \xi_i^{n+1} - \frac{\kappa_i}{c_{v,i}^4} (u_i^{n+1})^4 \right). \quad (44)$$

Here the term to solve for is

$$X = \rho_i \xi_i^{n+1} - \frac{a}{\kappa_i} \frac{\kappa_i}{c_{v,i}^4} (u_i^{n+1})^4. \quad (45)$$

Defining the quantities

$$\begin{aligned} c_1 &= \rho_i \xi_i^n - \frac{1}{2} \frac{dt}{N} ac \rho_i \left(\frac{\rho_i \kappa_i}{a} \xi_i^n - \frac{\kappa_i}{c_{v,i}^4} (u_i^n)^4 \right), \\ c_2 &= \frac{\kappa_i a}{c_{v,i}^4 \kappa_i}, \\ c_3 &= u_i^n + \frac{1}{2} \frac{dt}{N} ac \left(\frac{\rho_i \kappa_i}{a} \xi_i^n - \frac{\kappa_i}{c_{v,i}^4} (u_i^n)^4 \right), \end{aligned}$$

$$\begin{aligned}
c_4 &= \frac{1}{2} \frac{dt}{N} a c \rho_i \frac{\kappa_i}{a}, \\
c_5 &= \frac{1}{2} \frac{dt}{N} a c \frac{\kappa_i}{a},
\end{aligned} \tag{46}$$

the equation to be solved becomes

$$X^4 + \frac{4c_3}{c_5} X^3 + \frac{6c_3^2}{c_5^2} X^2 + \left(\frac{4c_2 c_3^3}{c_5^2} + \frac{c_4}{c_2 c_5^4} + \frac{1}{c_2 c_5^4} \right) X + \frac{(c_2 c_3^4 - c_1)}{c_2 c_5^4} = 0, \tag{47}$$

which can be solved using any method for solving quartic equations (see Appendix A for the analytical method). While it is possible to use a numeric solver, e.g. a Newton-Raphson method, we have found that the analytic solution is to be preferred since tests show it is much quicker. One minor difficulty when calculating the analytic solution is that while two of the roots of a quartic equation (usually) contain an imaginary component and can readily be discarded, the code must be able to distinguish between the two real roots. We choose the correct solution as the one which gives a new gas temperature that lies between the old values of T_g and T_r . In the case of four real roots, the same test can be applied. Four complex roots usually indicates that the timestep is too large.

If the real root chosen is denoted by X_1 , the quantity $\frac{\kappa_i}{a} X_1$ should be substituted back into equations 43 and 44 as the term $\left(\frac{\rho_i \kappa_i}{a} \xi_i^{n+1} - \frac{\kappa_i}{c_{v,i}^4} (u_i^{n+1})^4 \right)$ to provide the new radiation and gas energies. We have found that solving for X_1 as $\rho_i \xi_i^{n+1} - \frac{a}{\kappa_i} \frac{\kappa_i}{c_{v,i}^4} (u_i^{n+1})^4$ rather than $\left(\frac{\kappa_i}{a} \rho_i \xi_i^{n+1} - \frac{\kappa_i}{c_{v,i}^4} (u_i^{n+1})^4 \right)$ can be more accurate if the numbers involved in the calculation are closer to the order of unity, ensuring that the range does not fall outside the Fortran DOUBLE PRECISION variable bounds. For different values of opacity it may even be desirable to solve for $\frac{a}{\kappa} X$ or even $(\frac{a}{\kappa})^2 X$ depending on the problem. The code can be made adaptive in this respect by checking that the co-efficient of the first-order term in equation 47 is smaller than the fourth root of the largest allowed floating point number, and adapting the quantity to solve for accordingly.

The analytical solution of this quartic equation, whilst being much faster than a numerical solver, can fail when the number of sweeps is too small. In this case, the code detects a failure to reach a physical temperature and returns to the calling subroutine requesting a greater number of sweeps. This is a fairly common occurrence when the code is just starting, as the initial number of sweeps is an estimate input by the user.

3.2.5 The Adaptive Sweeping Scheme

The way the sweeping is performed is important, and can greatly affect the accuracy of the implicit method. Initially the quantities ξ and u are copied into arrays upon which the sweeping operations are to be performed. Then sweeping commences in the following order: First the flux-limiter λ_i is calculated for each particle, along with the Eddington factor f_i . The next step is to calculate the flux diffusion term for all $i - j$ particle pairs, update ξ , then calculate the radiation pressure term and update ξ again. Independent of the radiation energy calculations, the sound speeds c_s (used in the SPH viscosity) are calculated, followed by the gas pressure/viscosity term and u is updated. The sweep ends with the interaction term between u and ξ , after which the next sweep commences with the calculation of the flux-limiter using the new values of ξ and u . Once the specified number of sweeps are complete the temporary arrays are copied back into their normal counterparts.

Since it is not known *a priori* how many sweeps are required to reach a certain accuracy, we use an Adaptive Sweeping Scheme (ASS) to determine the necessary number of sweeps. The code begins by trying an initial number of sweeps 2^m (where m is an integer, $m > 0$). The implicit subroutine is called twice, once for 2^{m-1} sweeps and once for 2^m sweeps. If the fractional error in both ξ and u for all particles between the two sweeps is less than a specified tolerance the values of ξ and u from the 2^m sweep calculation are used, and m is decreased by unity for the next timestep to allow the code to adapt if fewer sweeps are required. We found that a tolerance of 10^{-3} gave a good trade off between accuracy and speed and this value is used for all the test calculations presented in this paper. If the error is above the tolerance, m is incremented by unity, and the method repeats until either an acceptable solution is found, or too many sweeps are attempted. The trapezoidal scheme is such that doubling the number of sweeps typically halves the errors. The ASS can be optimized to take this into account, e.g. if the maximum error is one quarter of the acceptable tolerance the number of sweeps can be reduced by a factor of four for the next timestep. If at any time the implicit integration would take ξ or u negative, the implicit routine immediately returns to ASS with a message to double the number of sweeps, similar to what occurs when the quartic solver fails.

It is also desirable for two-step integrators like the Runge-Kutta-Fehlberg or predictor-corrector integrators that require the calculation of quantities at both the half and the full timesteps to use two independent numbers of sweeps. Typically, the full timestep call of the implicit method requires twice as many sweeps.

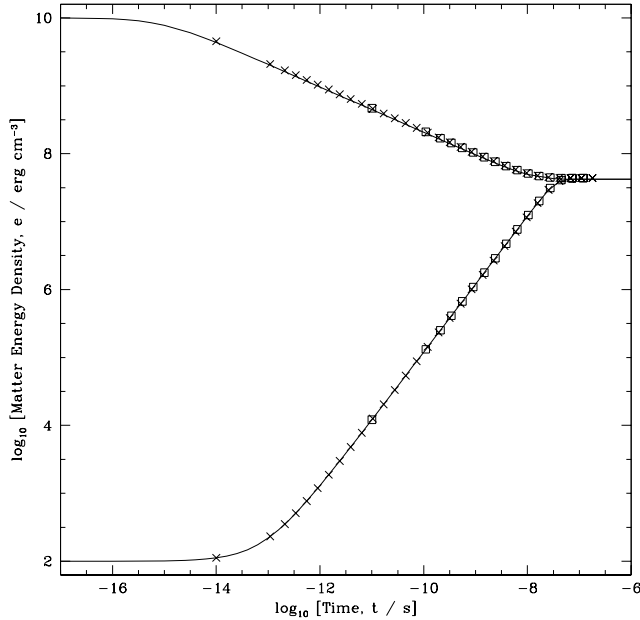


Figure 1. The evolution of the gas energy density e as it equilibrates with a radiation energy density $E = 10^{12}$ erg cm $^{-3}$. In the upper case, $e = 10^{10}$ erg cm $^{-3}$ initially, while in the lower case $e = 10^2$ erg cm $^{-3}$. The solid line is the analytic solution, the crosses are the results of the SPH code using implicit timesteps of the greater of 10^{-14} s or five percent of the elapsed time, and the squares with a timestep of the larger of 10^{-11} s or five percent of the elapsed time. The symbols are plotted every ten timesteps.

4 TEST CALCULATIONS

4.1 Heating and cooling terms

As in Turner & Stone (2001) we tested the interaction between the radiation and the gas to check that the temperatures of the gas and the radiation equalise when $T_g \neq T_r$ initially. A gas was set up so that there was no initial velocity, with a density $\rho = 10^{-7}$ g cm $^{-3}$, opacity $\kappa = 0.4$ cm 2 g $^{-1}$, and $\gamma = \frac{5}{3}$ and $E = 10^{12}$ ergs cm $^{-3}$. Two tests were carried out, one where the gas heated until it reached the radiation temperature, and one where it cooled. The first test had $e = u\rho = 10^2$ ergs cm $^{-3}$, and the second $e = u\rho = 10^{10}$ ergs cm $^{-3}$. The boundaries of the calculation used reflective ghost particles, and the position of the boundary was fixed.

This problem can be approximated by the differential equation

$$\frac{de}{dt} = c\kappa E - a\kappa \left(\frac{e}{\rho c_v} \right)^4, \quad (48)$$

in the case where the energy in the radiation is much greater than that in the gas. In figure 1, the solid line is this analytic solution, plotted both for the cases where T_g increases and decreases. The crosses are the results of the SPH code using an implicit timestep that is set to the larger of 10^{-14} s or five percent of the time elapsed. The squares are similar, but with a timestep being the greater of 10^{-11} s or five percent of the time elapsed. As can be seen, the match between the analytic solution and the solutions given by the SPH code is excellent.

4.2 Propagating radiation in optically thin media

In the standard diffusion approximation, radiation can, in optically thin regions, approach infinite velocity. This is unphysical, and the flux limiter has been introduced to limit the diffusion of radiation to the speed of light. To examine how well our code limits the speed of the radiation, a one centimetre long one-dimensional box is filled with 100 equally spaced SPH particles, with $E = 10^{-2}$ erg cm $^{-3}$ ($\xi = 0.4$ erg g $^{-1}$), $\rho = 0.025$ g cm $^{-3}$ and $\kappa = 0.4$ cm 2 g $^{-1}$. Initially, the radiation and gas are in thermal equilibrium.

At the start of the simulation, the radiation energy density for the leftmost ten particles was changed to $E = 0.1$ erg cm $^{-3}$ ($\xi = 4$ erg g $^{-1}$) and the resulting radiation front was allowed to propagate across the region. The ghost particles were reflective except in specific radiation energy ξ , which was fixed equal to $\xi = 4$ erg g $^{-1}$ at the left hand boundary and $\xi = 0.4$ erg g $^{-1}$ at the right. The implicit code was used with various timesteps ranging from an explicit timestep to a single implicit

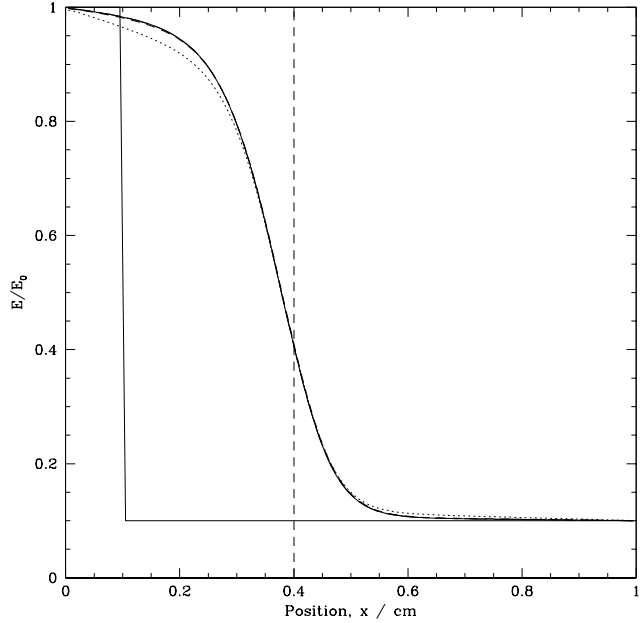


Figure 2. The propagation of a radiation pulse across a uniform medium. The time is $t = 10^{-11}$ s. The vertical dashed line shows the expected position of the pulse based on the speed of light. The results are essentially independent of the size of the implicit timestep used. Results are given for implicit timesteps equal to (solid line), ten times (dotted line), and one hundred times (dashed line) the explicit timestep. The dot-dashed line gives the result using a single implicit step of 10^{-11} s. The results for the explicit code are identical to that of the implicit code using the explicit timestep, and hence are not plotted. The initial conditions are also shown (solid line).

step lasting 10^{-11} s. The results are shown in figure 2. The result for the explicit code lies on top of the result for the implicit code using an explicit timestep.

As can be seen, the radiation pulse propagates at the correct speed, even using a single implicit timestep that is more than 10^4 times the explicit timestep. The front is smoothed out in a manner similar to the results of Turner & Stone (2001); both methods are quite diffusive in this situation. We note Turner & Stone (2001) began with an initial discontinuity in the radiation energy density of 21 orders of magnitude. We found that as the discontinuity increases in magnitude, the radiation pulse propagates more slowly with SPH due smoothing of the gradient of E and the consequent error in the value of the flux-limiter.

4.3 Optically-thick (adiabatic) and optically-thin (isothermal) shocks

A shock-tube test was set up to investigate the way the code simulated optically-thin and optically-thick regimes and the transition between them. In the limit of high optical depth, the gas cannot cool because the radiation is trapped within the gas; thus the shock is adiabatic. An optically-thin shock, on the other hand, is able to efficiently radiate away the thermal energy and thus behaves as an isothermal shock. In these shock tests, the gas and radiation are highly coupled and, thus, their temperatures are equal.

A domain 2×10^{15} cm long extending from $x = -1 \times 10^{15}$ to 1×10^{15} cm was set up, with an initial density of $\rho = 10^{-10}$ g cm $^{-3}$, and the temperatures of the gas and radiation were initially 1500 K. One hundred particles were equally spaced in the domain, with those with negative x having a velocity equal to the adiabatic ($\gamma = 5/3$) sound speed $v_0 = c_s = 3.2 \times 10^5$ cm s $^{-1}$, and those with positive x travelling at the same speed in the opposite direction. The two flows impact at the origin, and a shock forms. Opacities of $\kappa = 40, 0.4, 4.0 \times 10^{-3}$ and 4.0×10^{-5} cm 2 g $^{-1}$ were used to follow the transition from adiabatic to isothermal behaviour. Ghost particles were placed outside the boundaries and maintain the initial quantities of their respective real particles. The boundaries moved inwards with the same velocities as the initial velocities of the two streams.

The adiabatic and isothermal limits can be solved analytically (e.g. Zel'dovich & Raizer 2002). The shock speed is given by

$$D = \frac{(\gamma_{\text{eff}} - 3) + \sqrt{(\gamma_{\text{eff}} + 1)^2 v_0^2 + 16\gamma_{\text{eff}}}}{4}, \quad (49)$$

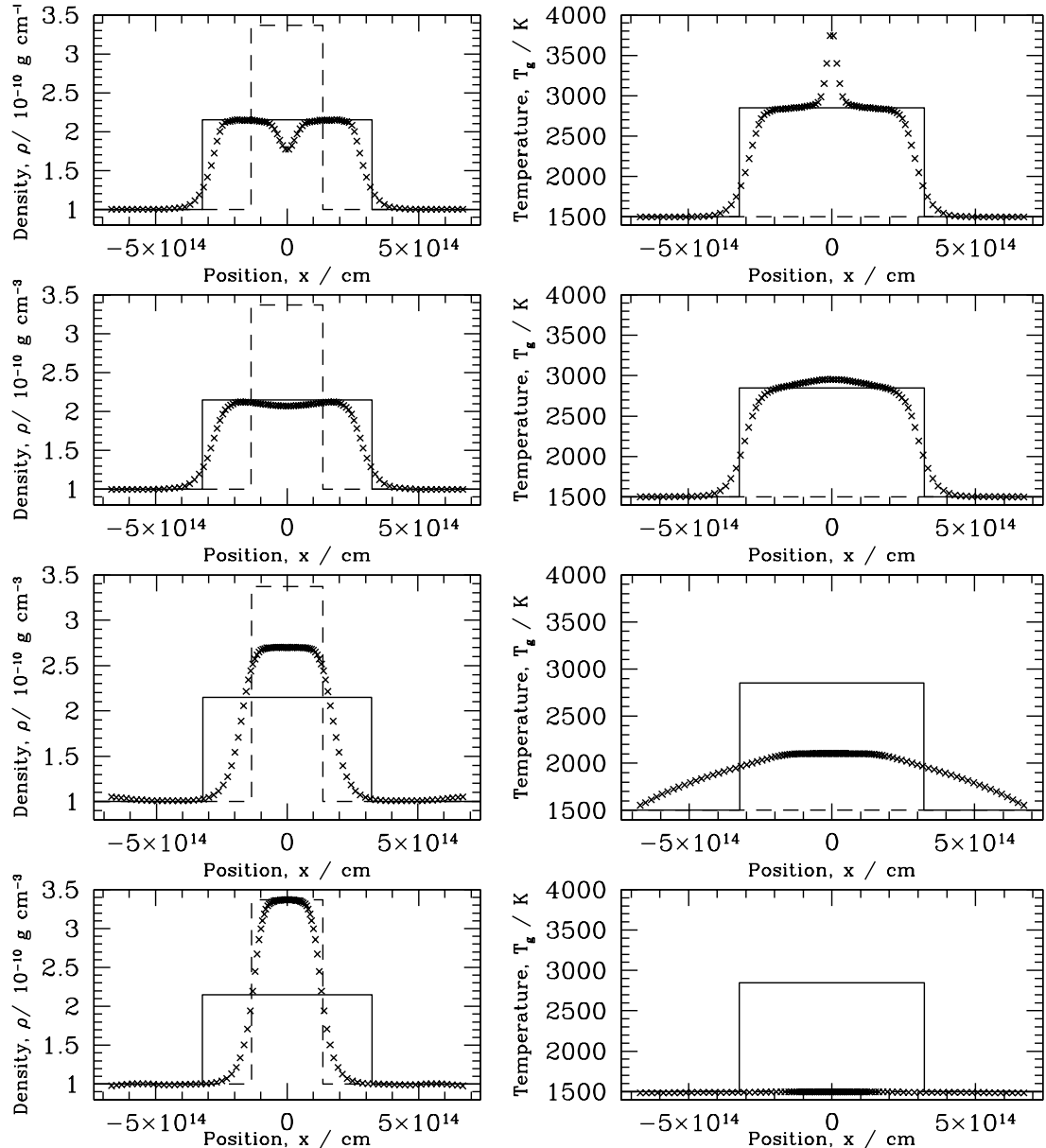


Figure 3. A set of shocks with differing opacity at time $t = 1.0 \times 10^9$ s. Density is on the left, and gas temperature on the right. The crosses are the SPH results; the solid line gives the analytic solution for an adiabatic shock, and the dashed line for an isothermal shock. The opacities are (top) $\kappa = 40$, (upper middle) $\kappa = 0.4$, (lower middle) $\kappa = 4.0 \times 10^{-3}$ and (bottom) $\kappa = 4.0 \times 10^{-5} \text{ cm}^2 \text{ g}^{-1}$. As the opacity is decreased, the shocks transition from adiabatic to isothermal behaviour.

where $\gamma_{\text{eff}} = 5/3$ for the adiabatic case, and $\gamma_{\text{eff}} = 1$ for the isothermal case. The ratio of the final to the initial density is given by

$$\frac{\rho_1}{\rho_0} = 1 + \frac{v_0}{D}, \quad (50)$$

and, for the adiabatic shock, the ratio of the final to the initial temperature is given by

$$\frac{T_1}{T_0} = \frac{\rho_1}{\rho_0} + \frac{v_0 D \rho_0}{\rho_0}. \quad (51)$$

These analytic solutions are shown by the solid and dashed lines in figure 3. In the figure, the opacity decreases from top to bottom showing the transition from optically-thick (adiabatic) to optically-thin (isothermal) behaviour. The extremes are in good agreement with their respective analytic adiabatic and isothermal solutions. Note that the spike in thermal energy near the origin and the corresponding reduction in density for the optically-thick case (due to ‘wall-heating’) is softened by the radiation transport that occurs in the intermediate opacity calculation with $\kappa = 0.4$.

Where possible, comparison shows that the results from a fully explicit calculation are virtually identical to those obtained

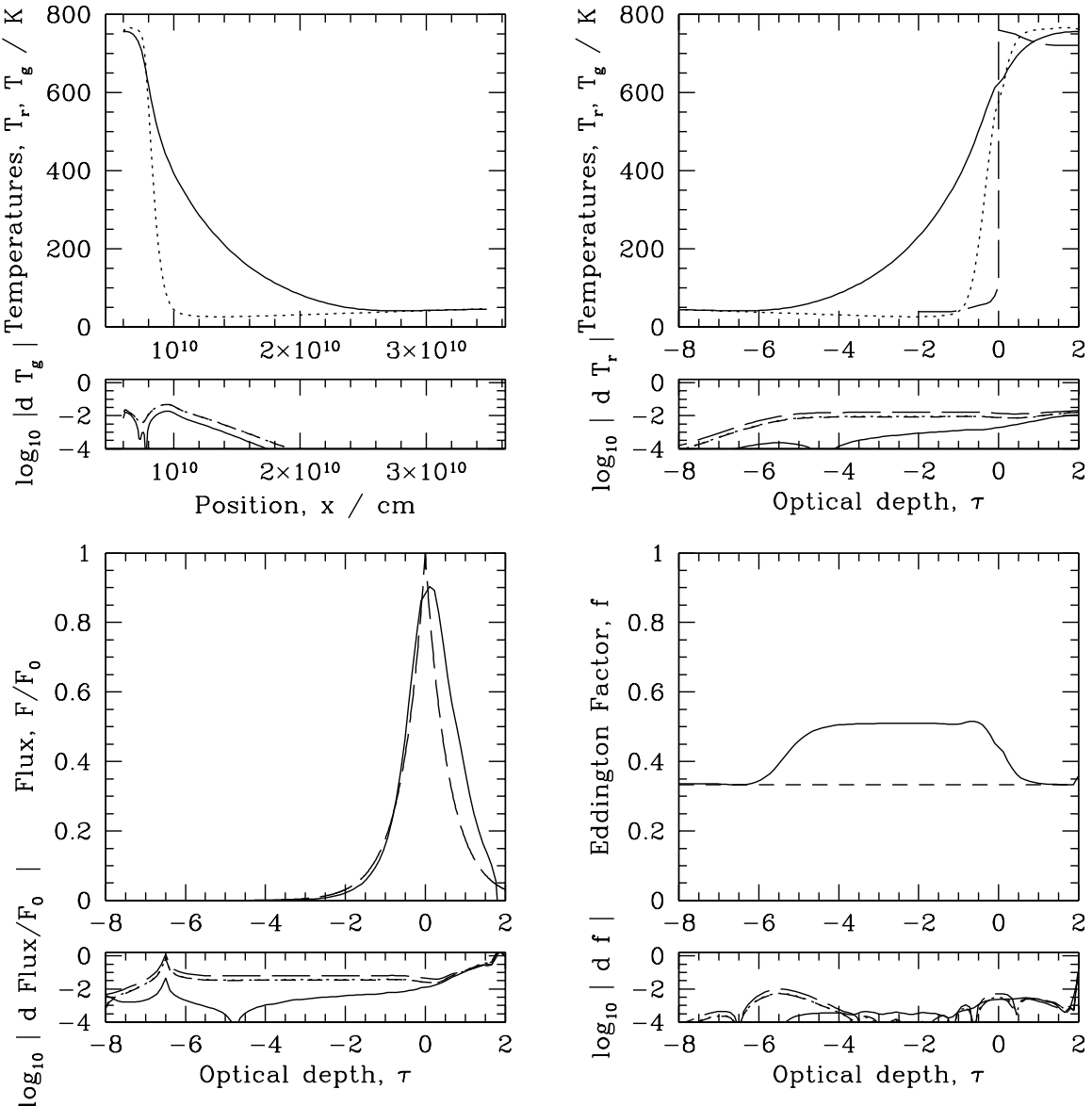


Figure 4. The sub-critical shock, with piston velocity $6 \times 10^5 \text{ cm s}^{-1}$ and 100 particles. The large panels show the results using the explicit code. The top panels show radiation (solid line) and gas (dotted line) temperatures. The bottom left panel shows the normalised flux and bottom right panel the Eddington factor. The long-dashed lines give the analytic solutions for the gas temperature and normalised flux. An Eddington factor of $1/3$ is also indicated for reference (short-dashed line, lower right panel). The subpanels plot the logarithm of the difference between the results using the explicit code and the implicit code (see the main text). The implicit code was run with timesteps of 1 (solid line), 10 (short-dashed line), and 100 (dotted line) times the explicit timestep and with a hydrodynamical timestep (long dashes).

implicitly. However, as the opacity is increased, the implicit code offers an enormous improvement in speed because the explicit timestep is set by the interaction term between the radiation and gas (equations 32 and 33) which is inversely proportional to the opacity. With an opacity of $\kappa = 4.0 \times 10^{-5}$, the codes are similar in speed. However, the implicit code is ~ 100 times faster than the explicit when $\kappa = 4.0 \times 10^{-3}$, and $\sim 10^4$ times faster when $\kappa = 0.4$. For $\kappa = 40$, we could not run an explicit calculation, but the implicit code is likely to be $\sim 10^6$ times faster.

4.4 Sub- and super-critical shocks

A supercritical shock occurs when the photons generated by a shock have sufficient energy to preheat the material upstream. The characteristic temperature profile of a supercritical shock is where the temperature on either side of the shock is sim-

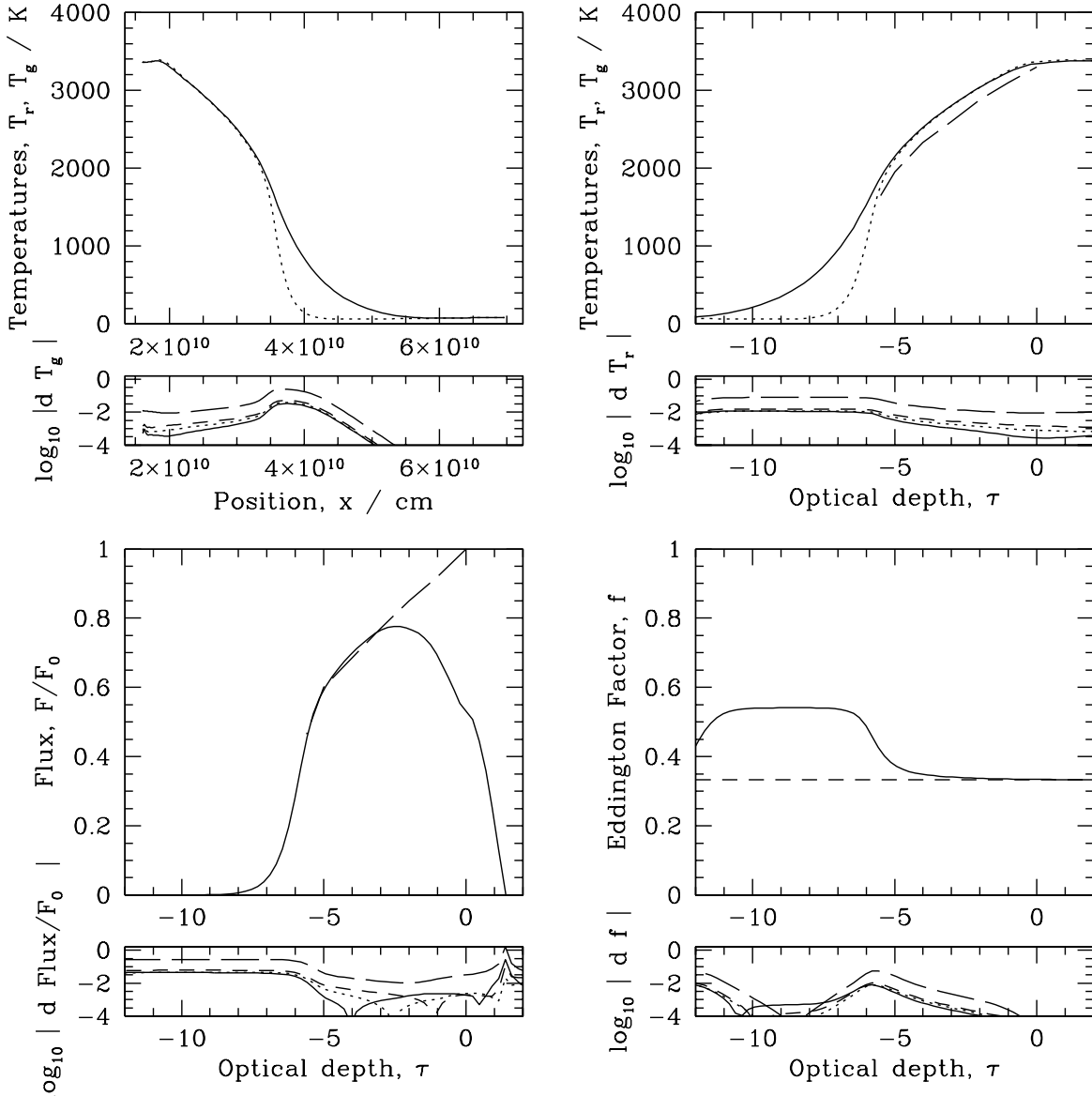


Figure 5. The super-critical shock, with piston velocity $1.6 \times 10^6 \text{ cm s}^{-1}$ and 100 particles. This shock is strong enough for radiation from the shock to preheat the gas upstream. See figure 4 for more details.

ilar, rather than the downstream temperature being much higher than the upstream, as occurs in a subcritical shock (see Zel'dovich & Raizer 2002, for more details).

The initial conditions of this problem are those of Sincell, Gehmeyr & Mihalas (1999) and Turner & Stone (2001). A gas with opacity $\kappa = 0.4 \text{ cm}^2 \text{ g}^{-1}$, uniform density $\rho = 7.78 \times 10^{-10} \text{ g cm}^{-3}$, mean molecular weight $\mu = 0.5$ and $\gamma = \frac{5}{3}$ is set up with ξ and u in equilibrium, with a temperature gradient of $T = 10 + (75x/7 \times 10^{10}) \text{ K}$. Initially the particles are equally spaced between $x = 0$ and $x = 7 \times 10^{10} \text{ cm}$ for the supercritical shock, and between $x = 0$ and $x = 3.5 \times 10^{10} \text{ cm}$ for the subcritical shock. At time $t = 0$ a piston starts to move into the fluid from the left-hand boundary (simulated by moving the location of the boundary). For the subcritical shock the piston velocity is $v_p = 6 \text{ km s}^{-1}$, and for the supercritical shock $v_p = 16 \text{ km s}^{-1}$, as per Sincell et al. (1999). The ghost particles are reflective in the frame of reference of the boundary. Artificial viscosity parameters $\alpha_v = 2$ and $\beta_v = 4$ were used to smooth out oscillations.

The results of calculations using 100 particles are shown in figure 4 for the sub-critical shock and in figure 5 for the super-critical shock. The top left panel for each shows the temperature of the radiation field (solid line) and the gas (dotted line) against position, and the top right shows the same quantities against optical depth τ , with $\tau = 0$ set at the shock front (measured from the density distribution). The bottom left panel shows normalised flux, and the bottom right the value of the Eddington factor. The analytic solutions discussed by Sincell et al. (1999) and Zel'dovich & Raizer (2002) for the temperatures

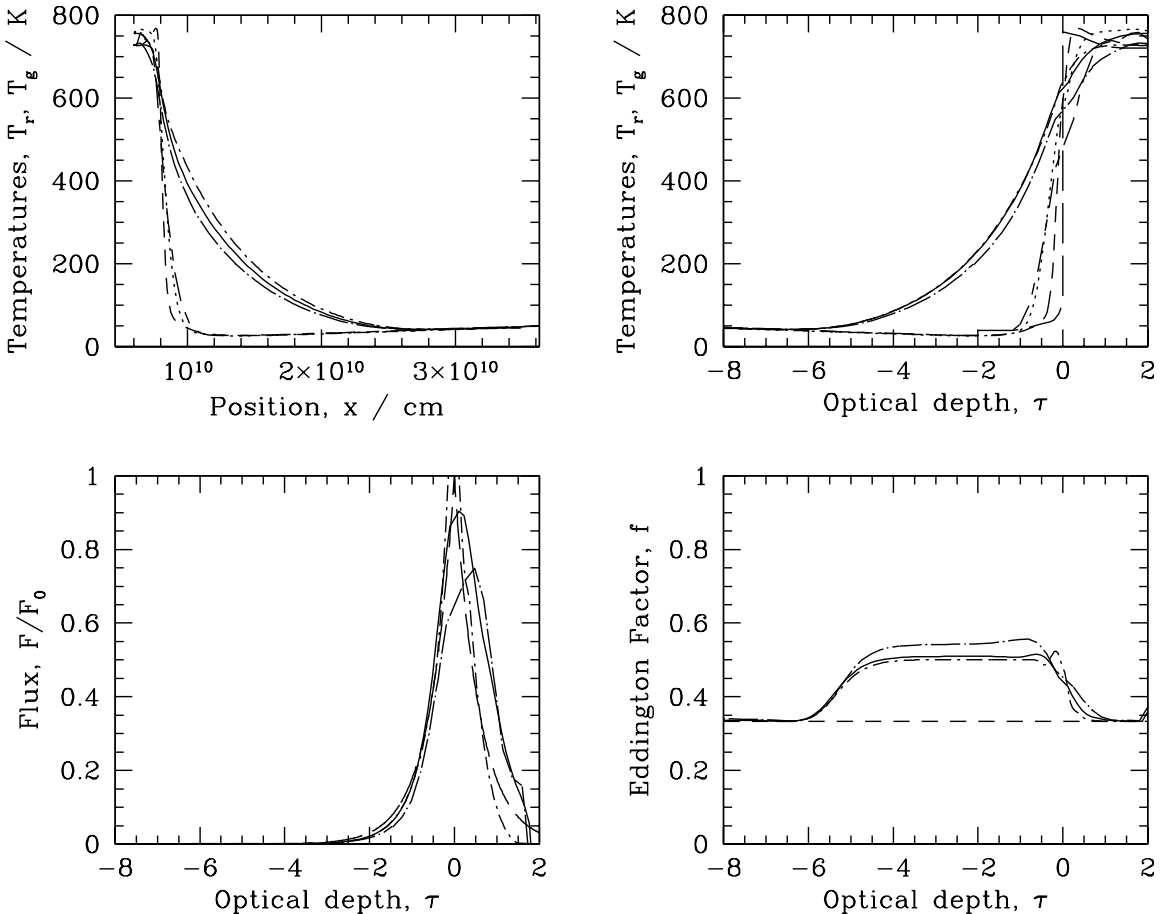


Figure 6. The sub-critical shock with differing resolutions. For 50 particles, the dot-long-dashed lines give the radiation temperature, the flux, and the Eddington factor while the short-dash-long-dashed lines give the gas temperature. For 100 particles, the solid lines give the radiation temperature, the flux, and the Eddington factor while the dotted lines give the gas temperature. For 250 particles, the dot-short-dashed lines give the radiation temperature, the flux, and the Eddington factor while the short-dashed lines give the gas temperature. The analytic solution is given by the long-dashed lines.

and fluxes of the shocks are shown with long-dashed lines. Figures 4 and 5 are plotted using the explicit code. In subpanels beneath the main panels, we compare the results from the implicit code with the explicit results. Calculations were performed using the implicit code with timesteps of 1, 10, and 100 times the explicit timestep and with a timestep limited only by the hydrodynamical timestep criteria (equations 28 and 29). In the subpanels, we plot the differences of the implicit results with respect to the explicit results. We divide the difference between the implicit and explicit values by the explicit value to obtain a fractional error and take the logarithm of the absolute value of this fraction. Thus, a difference of -2 on the subpanels corresponds to an error of 1 percent with respect to the explicit result.

Figures 6, 7 and 8 show the effect on the shocks of changing the resolutions. For the sub-critical shock, the results converge towards the analytic solutions for both the gas temperature and the flux as the particle number is increased. Note that our highest resolution case has the same number of particles per unit length as Turner & Stone (2001) have grid cells. Increasing the resolution of the super-critical shock has less of an effect on the results, although the flux in the vicinity of the shock improves, and the spike in gas temperature at the location of the shock is better resolved (c.f. figure 8).

Both the explicit and implicit codes model the sub-critical and super-critical shocks well. With similar resolution, our results are in good agreement with those of Turner & Stone (2001), although we note that Turner & Stone (2001) only used timesteps as large as ten radiation diffusion times. However, we found that in these tests, our implicit code offers little advantage over the explicit code. With the super-critical shock and an implicit timestep 10 times longer than the explicit timestep, the speed is similar, but using a hydrodynamic timestep the code is roughly 10 times slower. For the sub-critical shock, the situation is worse. Running with an implicit timestep 100 times longer than the explicit timestep takes ≈ 60 times longer and implicit calculation using a hydrodynamical timestep takes ≈ 400 times longer than an explicit calculation. The decrease in speed is due to the large number of sweeps required by the implicit integration scheme in order to achieve the

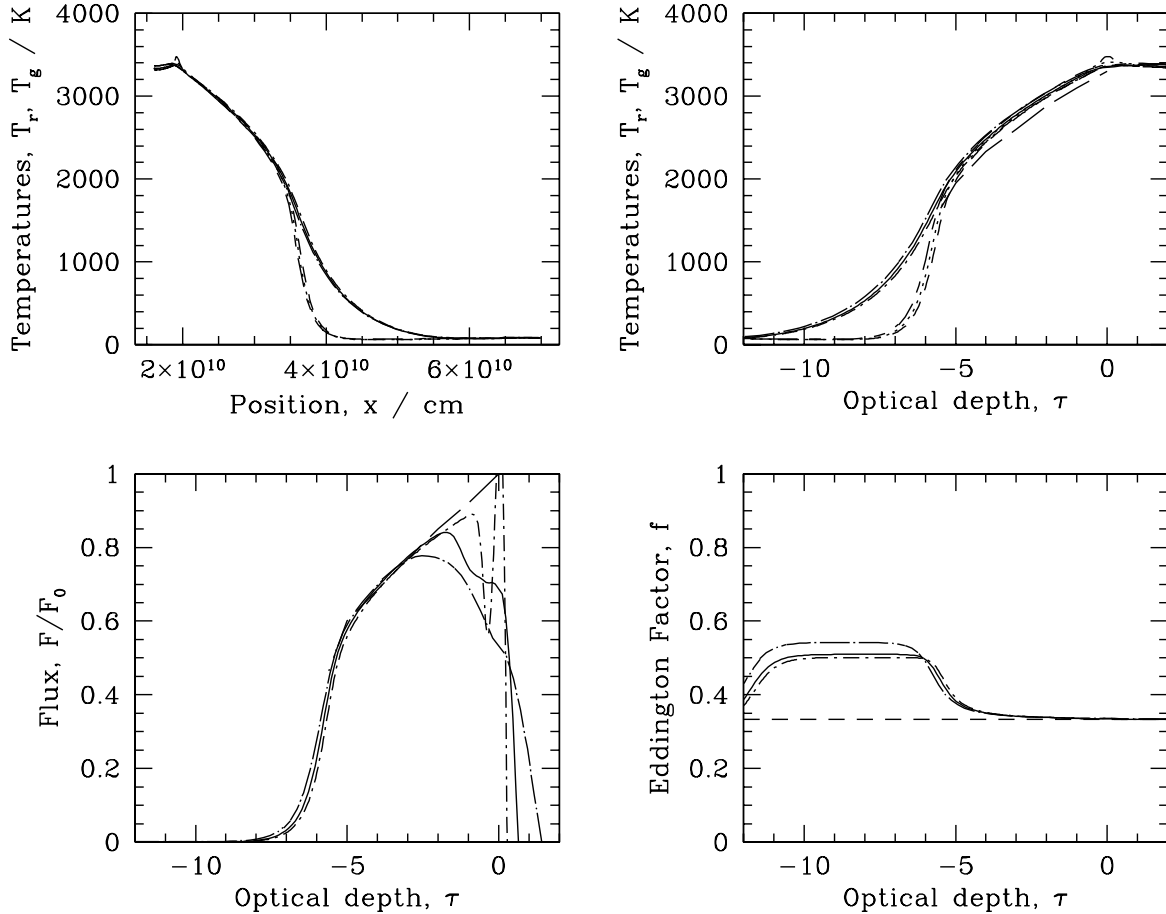


Figure 7. The super-critical shock with differing resolutions. For 100 particles, the dot-long-dashed lines give the radiation temperature, the flux, and the Eddington factor while the short-dash-long-dashed lines give the gas temperature. For 200 particles, the solid lines give the radiation temperature, the flux, and the Eddington factor while the dotted lines give the gas temperature. For 500 particles, the dot-short-dashed lines give the radiation temperature, the flux, and the Eddington factor while the short-dashed lines give the gas temperature. The analytic solution is given by the long-dashed lines.

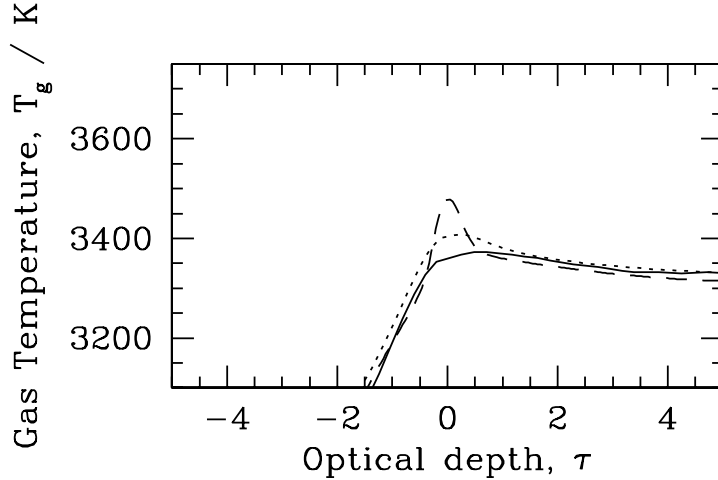


Figure 8. A zoom-in of the spike for the supercritical shock. We plot the results with 100 (solid line), 200 (dotted line) and 500 (dashed line) particles. As expected, the spike is more obvious with higher resolution.

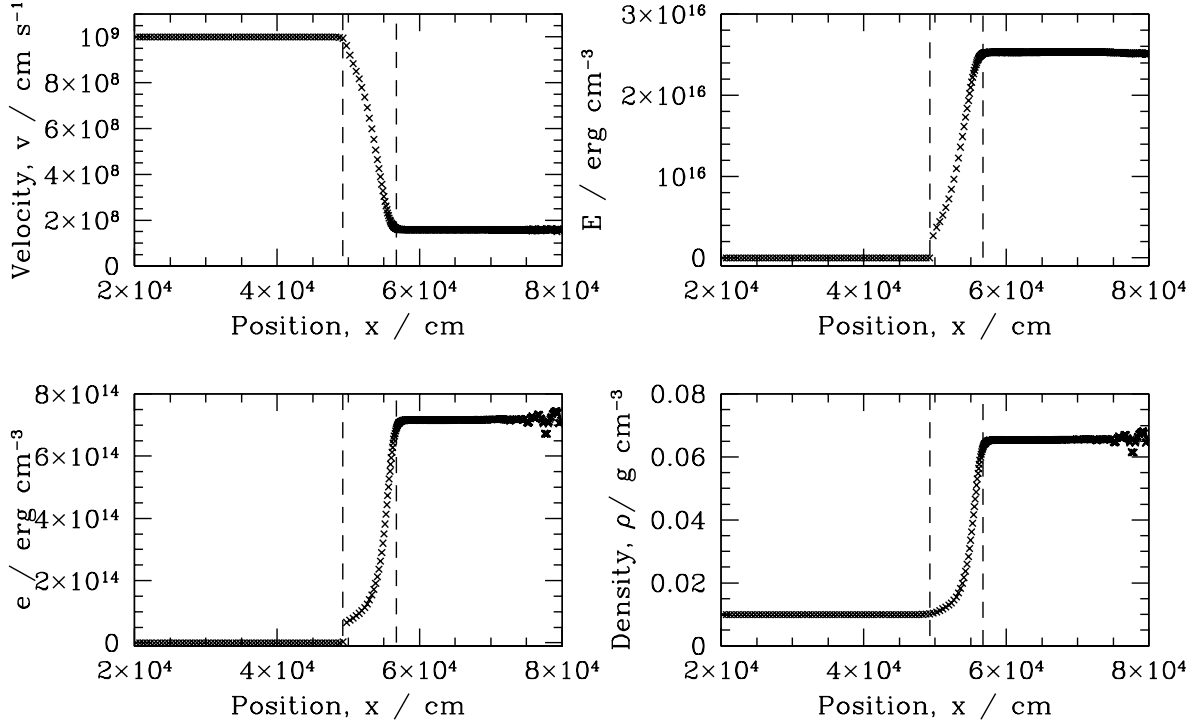


Figure 9. The radiation-dominated shock at time $t = 5 \times 10^{-4}$ s. We plot the velocity, radiation and gas energy densities and gas density versus position. The vertical dashed lines show the expected shock thickness. Gas flows into the shock from the left. The after effects of the transient that occurs at the start of the calculation can be seen at the far right of the plots.

required accuracy. Increasing the tolerance above 10^{-3} results in quicker calculations, roughly inversely proportional to the tolerance, however the solution is less accurate and both the temperatures of the gas and radiation are overestimated.

4.5 Radiation-dominated shock

In material of high optical depth the radiation generated in a shock cannot diffuse away at a high rate, and so the radiation becomes confined in a thin region adjacent to the shock. Turner & Stone (2001) performed a calculation that tests whether the shock thickness is what one would expect in these circumstances. An extremely high Mach number shock (Mach number of 658) is set up, with the gas on the left having an initial density of $\rho = 0.01 \text{ g cm}^{-3}$ (set by using different mass particles), opacity $\kappa = 0.4 \text{ cm}^2 \text{ g}^{-1}$, temperature $T_r = T_g = 10^4 \text{ K}$, and speed 10^9 cm s^{-1} . The gas on the right has density $\rho = 0.0685847 \text{ g cm}^{-3}$, opacity $\kappa = 0.4 \text{ cm}^2 \text{ g}^{-1}$, temperature $T_r = T_g = 4.239 \times 10^7 \text{ K}$, and speed $1.458 \times 10^8 \text{ cm s}^{-1}$. The locations of the boundaries move with the same speed as their respective particles, and the properties of the ghost particles outside these boundaries are fixed at their initial values. We use the implicit code with a timestep 100 times larger than the explicit timestep. 1500 particles are equally spaced over a domain extending from $x = -6 \times 10^5 \text{ cm}$ to $x = 1.5 \times 10^5 \text{ cm}$ initially, with the discontinuity at $x = 0.5 \times 10^5 \text{ cm}$. The location of the shock should be fixed in this frame, although individual particles flow through the shock.

After a period where a transient feature forms at the shock front and drifts downstream with the flow, a stable shock is established. Its thickness is expected to be roughly equal to the distance $l = c\lambda/\kappa\rho u_1$, where u_1 is the speed of material flowing into the shock front.

Figure 9 shows the results at a time $t = 5 \times 10^{-4}$ s, of the radiation energy density E , gas energy density e , velocity v , and density ρ versus position. The vertical dashed lines indicate the expected shock thickness and the SPH results are in good agreement. The after-effects of the transient moving downstream can be seen on the right of the plots of density and gas energy density. The explicit code takes roughly a factor of ten times longer than the implicit code for this test.

5 CONCLUSIONS

In this paper, we have presented a method for including radiative transfer in the flux-limited diffusion approximation in a smoothed particle hydrodynamics (SPH) code. The energy equations may be integrated either explicitly or implicitly. By integrating the energy equations implicitly the short timesteps due to the rapid propagation of radiation can be avoided and timesteps limited only by hydrodynamical processes can be used. In problems where the temperatures of the gas and radiation are equal, the implicit code loses little in accuracy but may be many orders of magnitude faster than an explicit calculation. However, in cases where the two temperatures are not equal the implicit scheme may actually be slower due to the large number of sweeps required to obtain an accurate solution.

Overall, the SPH code performs as accurately as the ZEUS code with radiative transfer in the flux-limited diffusion approximation as described by Turner & Stone (2001). Although the code and test calculations presented here are one-dimensional, it is straightforward to implement the radiation hydrodynamical equations in a three-dimensional SPH code due to the fact that the SPH method is structured around interactions between pairs of particles. In going from one to two or three dimensions, the general method is the same. The main difference is that the radiation pressure term in the evolution equation for the specific radiation energy involves a more complicated tensor equation. Aside from this, the major limitation associated with increasing the number of dimensions is that more particles are required to obtain the same resolution, thus more computational effort is required. Three-dimensional calculations will be presented in a subsequent paper. We plan to use this method to investigate the effects of radiative transfer on star formation. Other applications include modelling phenomena such as accretion discs and radiation-dominated flows.

ACKNOWLEDGMENTS

The authors are grateful to Neal Turner and Jim Stone for discussions regarding test calculations for radiation hydrodynamics and critical readings of the manuscript, and Charles D. H. Williams for discussions on implicit integration techniques. SCW acknowledges support from a PPARC postgraduate studentship.

APPENDIX A: THE ANALYTIC SOLUTION OF A QUARTIC EQUATION

To solve the quartic equation $x^4 + a_3x^3 + a_2x^2 + a_1x + a_0 = 0$, it is necessary to first find the real root y_1 of the resolvent cubic

$$y^3 - a_2y^2 + (a_1a_3 - 4a_0)y + (4a_2a_0 - a_1^2 - a_3^2a_0) = 0, \quad (\text{A1})$$

either analytically or numerically. The algorithm for a real root (of which there must be at least one) can be obtained from a mathematical manipulation package and output as computer code to be copied into a program. The four roots of the quartic are then given by the four solutions of

$$z^2 + \left[\frac{a_3}{2} \mp \left(\frac{a_3^2}{4} + y_1 - a_2 \right)^{\frac{1}{2}} \right] z + \left[\frac{y_1}{2} \mp \left(\frac{y_1}{2} \right)^2 - a_0 \right]^{\frac{1}{2}} = 0, \quad (\text{A2})$$

(Abramowitz & Stegun 1972). If some of the coefficients are large and of roughly equal size it may be necessary to Taylor expand the relevant portion of the equation to maintain accuracy.

REFERENCES

Abramowitz M., Stegun I. A., 1972, Handbook of Mathematical Functions with Formulas, Graphs, and Mathematical Tables, 10th printing. Dover, New York

Balsara, D. 1989, Doctoral thesis, University of Illinois

Benz W., Cameron A. G. W., Press W. H., Bowers R. L., 1990, ApJ, 348, 647

Black D. C., Bodenheimer P., 1975, Ap. J., 199, 619

Brookshaw L., 1985, Proceedings of the Astronomical Society of Australia, 6, 207

Brookshaw L., 1986, Proceedings of the Astronomical Society of Australia, 6, 461

Cha S.-H., Whitworth A. P., 2003, MNRAS, 340, 73

Cha, S.- H. 2002, Doctoral thesis, University of Cardiff

Cleary P. W., Monaghan J. J., 1999, J. Comp. Phys., 148, 227

Dahlquist G., 1963, Nordisk Tidskrift for Informations Behandling, 3, 27

Evrard A. E., 1988, MNRAS, 235, 911

Flebbe O., Muenzel S., Herold H., Riffert H., Ruder H., 1994, *ApJ*, 431, 754

Gingold R. A., Monaghan J. J., 1977, *MNRAS*, 181, 375

Gingold R. A., Monaghan J. J., 1983, *MNRAS*, 204, 715

Hernquist L., Katz N., 1989, *Ap. J. Suppl.*, 70, 419

Inutsuka S., 1994, *Memorie della Societa Astronomica Italiana*, 65, 1027

Inutsuka S.-I., Imaeda Y., 2001, *Comp. Fluid. Dynam. J.*, 9, 316

Inutsuka, S.-I. 1998, in Shoken M., Miyama Kohji Tomisaka T.H., eds, *Astrophysics and Space Science Library*, Vol.240, *Numerical Astrophysics*, Proc. Int. Conf. on Numerical Astrophysics. Kluwer, Dordrecht, pp 367–374

Jubelgas M., Springel V., Dolag K., 2004, *astro-ph/0401456*

Levermore C. D., Pomraning G. C., 1981, *ApJ*, 248, 321

Lucy L. B., 1977, *AJ*, 82, 1013

Mihalas D., Mihalas B. W., 1984, *Foundations of Radiation Hydrodynamics*. Oxford University Press

Monaghan J. J., 1992, *Ann. Rev. Astron. Astrophys.*, 30, 543

Monaghan J. J., 1997, *J. Comp. Phys.*, 138, 801

Monaghan J. J., 2002, *MNRAS*, 335, 843

Morris J. P., Monaghan J. J., 1997, *J. Comp. Phys.*, 136, 41

Oxley S., Woolfson M. M., 2003, *MNRAS*, 343, 900

Price D. J., Monaghan J. J., 2004a, *MNRAS*, 348, 123

Price D. J., Monaghan J. J., 2004b, *MNRAS*, 348, 139

Sinell M. W., Gehmeyr M., Mihalas D., 1999, *Shock Waves*, 9, 391

Springel V., Hernquist L., 2002, *MNRAS*, 333, 649

Turner N. J., Stone J. M., 2001, *ApJS*, 135, 95

Watkins S. J., Bhattal A. S., Francis N., Turner J. A., Whitworth A. P., 1996, *A&AS*, 119, 177

Wood D., 1981, *MNRAS*, 194, 201

Zel'dovich Y. B., Raizer Y. P., 2002, *Physics of Shock Waves and High-Temperature Hydrodynamic Phenomena*, edited Hayes and Probstein. Dover, New York